

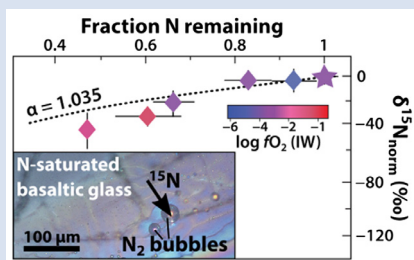
Nitrogen isotope fractionation during magma ocean degassing: tracing the composition of early Earth's atmosphere

C. Dalou^{1*}, C. Deligny¹, E. Füre¹



<https://doi.org/10.7185/geochemlet.2204>

Abstract



The evolution of the nitrogen concentration and isotopic composition during the degassing of Earth's magma ocean, and thus in the primitive atmosphere, is key to understanding how habitable conditions developed on Earth. To constrain nitrogen degassing from the magma ocean, we determined the variations of the N content at N₂ gas saturation, N speciation, and N isotopic composition of a magma ocean analogue (basaltic komatiite) at oxygen fugacities (*f*O₂) from IW–4.2 to IW (where IW is the logarithmic difference between experimental *f*O₂ and that at Fe–FeO equilibrium). We performed a series of N degassing experiments in a piston cylinder at 1.5 GPa and 1550 °C in pure forsterite capsules. N concentrations in the mafic silicate melts decreased from 13,481 ± 735 ppm under the most reducing conditions to 798 ± 4 ppm at IW, controlled by N speciation (as determined by Raman spectroscopy), which changed from nitride (±N–H complexes) to molecular N₂ with increasing *f*O₂. Nitrogen occurs solely as N₂ in the degassed gas, regardless of *f*O₂. Nitrogen isotopic compositions (as determined by secondary ion mass spectroscopy) became significantly lighter in the degassed melt (quenched glass), down to –41 ± 13 ‰ relative to the initial composition (measured in an undegassed sample), following open system degassing trends (variable with *f*O₂ conditions), indicative of Rayleigh fractionation. These findings imply that an atmosphere in equilibrium with a reduced magma ocean would be N-depleted, whereas with increasing magma ocean *f*O₂ conditions, the primitive atmosphere would have become more enriched in N₂ gas.

Received 11 May 2021 | Accepted 13 December 2021 | Published 19 January 2022

Introduction

The accretion of reduced building blocks during Earth's formation released enough energy to at least partially melt the Earth, forming one or more magma oceans (Elkins-Tanton, 2012). The evolving nitrogen abundance in the degassing magma ocean, and thus in Earth's early atmosphere, was fundamental to the development of habitable conditions and the maintenance of the terrestrial atmosphere and biosphere (Goldblatt *et al.*, 2009). Yet, the composition of Earth's early atmosphere remains debated: it is thought to have been either *i*) neutral to oxidising and composed of H₂O, CO₂, and N₂ if it resembled modern volcanic gases (Kasting, 1993), or *ii*) reducing and CH₄- and NH₃-rich if it degassed from the reduced materials that formed the Earth (Zahnle *et al.*, 2020), based on geochemical evidence that magma ocean degassing contributed to the formation of the Hadean atmosphere (see review by Gaillard *et al.*, 2021). Therefore, reconstructing nitrogen degassing during Earth's magma ocean stage(s) is critical to constraining the composition of the early atmosphere.

Nitrogen is often considered to be an inert molecule (N₂) and expected to behave somewhat like noble gases. However, recent works have shown that nitrogen is not always chemically inert and occurs as various species (N³⁻, NH₃, NH₂⁻, NH²⁻ and N₂) in silicate melts (Mikhail and Sverjensky, 2014; Dalou *et al.*, 2019a; Mosenfelder *et al.*, 2019; Boulliang *et al.*, 2020; Grewal

et al., 2020) and fluids (Li and Kepler, 2014). The speciation and solubility of nitrogen primarily depend on oxygen fugacity (Libourel *et al.*, 2003; Boulliang *et al.*, 2020; Bernadou *et al.*, 2021), which increased during the evolution of Earth's magma ocean (Frost *et al.*, 2008). Thus, the rate of nitrogen degassing and the reactions involved must have evolved similarly over geological time.

Nitrogen isotopic compositions, conventionally normalised to the present atmospheric value and reported as δ¹⁵N[‰] = $\left[\left(\frac{{}^{15}\text{N}/{}^{14}\text{N}_{\text{sample}}}{{}^{15}\text{N}/{}^{14}\text{N}_{\text{atm N}_2}} \right) - 1 \right] \cdot 1,000$, are useful for reconstructing Earth's N degassing history. For instance, the range of δ¹⁵N values observed in Archean diamonds corresponds to that in present day diamonds and mid-ocean ridge basalts (MORBs), implying that the mantle δ¹⁵N value has not evolved since the Archean (Cartigny and Marty, 2013). This is consistent with the observation that diffusion controlled N₂ degassing from the present day mantle, which is expected to preferentially segregate ¹⁴N into the atmosphere following Graham's law (*i.e.* the rate of diffusion/effusion of a gas is inversely proportional to the square root of its molecular weight; Javoy *et al.*, 1986), is limited to isotopic fractionations of 1–1.5 ‰ (Marty and Dauphas, 2003). However, Rayleigh models of equilibrium MORB degassing (Javoy *et al.*, 1986; Cartigny *et al.*, 2001) only consider the reaction N₂(magma) ↔ N₂(gas). This reaction has been experimentally determined at oxygen fugacity conditions (*f*O₂) > IW (Libourel

1. Université de Lorraine, CNRS, CRPG, F-54000 Nancy, France

* Corresponding author (email: celia.dalou@univ-lorraine.fr)



et al., 2003; Boulliung *et al.*, 2020), which applies to present day conditions of upper mantle degassing. However, because the integrated fO_2 during core formation was closer to IW-2 (Frost *et al.*, 2008), this reaction does not hold for the more reduced N species present in the magma ocean. Larger N isotopic fractionations are expected under reducing conditions at which N does not behave inertly. Therefore, quantifying N isotopic fractionations under conditions at which N dissolves in magmas as nitride or N-H complexes is prerequisite to quantitatively modelling the evolution of N concentrations and isotopic compositions during the formation of the Hadean atmosphere.

Degassing Experiments and Results

To establish the effect of fO_2 on the N degassing rate and identify N degassing reactions that may have occurred in the Earth's magma ocean, we determined the N concentration, speciation, and isotopic fractionation of a basaltic komatiite (used as magma ocean analogue melt) during degassing at 1.5 GPa and 1550 °C in pure forsterite capsules. Degassing experiments were performed using a series of Fe-free primitive basalts in which we explored fO_2 conditions ranging from IW to IW-4.2 (Table 1). These fO_2 conditions were not determined in the Fe-free experiments, but only estimated afterwards from the IW reaction in equivalent Fe-bearing runs (see Supplementary Information). The initial $^{15}N/^{14}N$ ratio of the starting material was 0.946 ± 0.003 , as determined in sample V133-PB4N2Si (Table 1), in which the initial N content was equal, within errors, to that measured after the experiment. Nitrogen was saturated in five experiments, as evidenced by bubbles in the quenched glass and/or surrounding forsterite (Fig. 1, Table 1).

The major element compositions of the silicate glasses were measured by electron microprobe (Table S-1). Nitrogen concentrations and $^{15}N/^{14}N$ ratios were determined by secondary ion mass spectrometry (SIMS) using the CAMECA IMS 1280-HR2 at the CRPG (Table 1). On each sample, four to six spot analyses of $^{14}N^{16}O^-$ and $^{15}N^{16}O^-$ were performed (see Supplementary Information). Measured N concentrations were homogeneous (*i.e.* with standard deviations below 10 %). N concentrations at 1.5 GPa and 1550 °C decreased from $13,481 \pm 735$ ppm (at IW-4.2) to 798 ± 4 ppm (at IW; Fig. 2a). In N saturated samples (as attested by the presence of bubbles), N concentrations decreased from $13,481 \pm 735$ ppm (at IW-4.2) to $3,084 \pm 377$ ppm (at IW-1). This decrease of N solubility with increasing fO_2 is consistent with observations in silicate melts at 1 atm (Libourel *et al.*, 2003; Boulliung *et al.*, 2020) and modelled at pressures up to 1 GPa (Bernadou *et al.*, 2021). Yet, the N solubilities observed herein are up to three orders of magnitude higher than those in a similar melt composition and at similar

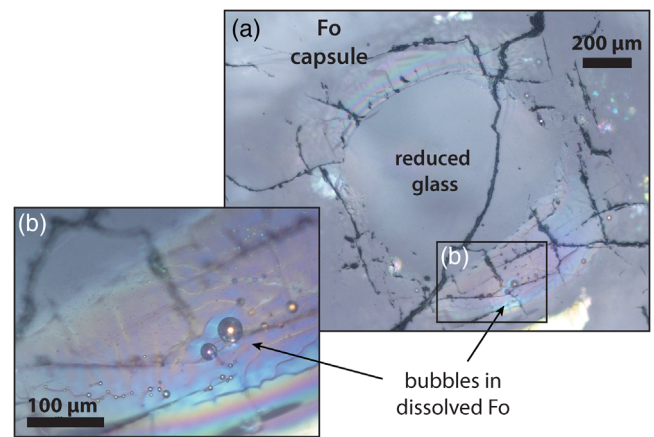


Figure 1 Optical microscope photograph of sample V125-PB8N, which contains $13,342 \pm 841$ ppm N and lost 15 % of its initial N content by degassing. The reduced glasses contain aligned microscopic bubbles, likely produced during quenching. Large bubbles, produced by degassing at high pressure and high temperature, are located within a rim of dissolved forsterite (Fo) at the border between the glass and the forsterite capsule. The dissolved forsterite contains negligible amounts of N (2 ± 2 ppm).

temperatures at 1 atm (Boulliung *et al.*, 2020) and one order of magnitude higher than those at 0.08 GPa (Bernardou *et al.*, 2021), consistent with the effect of pressure on N solubility described by Bernardou *et al.* (2021). The variation of N solubilities with fO_2 is directly related to changes of N speciation in the silicate melts, which were determined by Raman spectroscopy (see Supplementary Information). Around IW-4 and below, N is very soluble because it is dissolved as nitride, forming Si-N bonds with the silicate network; indeed, in very N-rich samples (>1 wt. % N), Si-N vibrations around 800 cm^{-1} were observed (Fig. 2b). In less reduced samples ($fO_2 > IW-4$), N is mostly dissolved as N-H complexes (Fig. 2c), and above IW-2, N is also dissolved as molecular N_2 (Fig. 2d). Consistent with previous studies (Mosenfelder *et al.*, 2019; Grewal *et al.*, 2020), N speciation in the silicate glasses controls N solubility variations with fO_2 conditions. Depending on initial N content and fO_2 , the fraction of N degassed varied from 7 to 53 %. Samples V152-PB0.5N and V149-PB1N did not show any evidence of degassing, *i.e.* no bubbles were observed in the glass or the forsterite rim, but lost 12 and 32 % of their initial N, respectively, likely due to diffusion through cracks formed in the forsterite capsule during compression.

The use of ^{15}N spiked samples permits us to obtain precise $^{15}N/^{14}N$ ratios in the silicate (with low uncertainties of 0.1 % on

Table 1 Experimental results on nitrogen contents and isotope fractionation in silicate glasses.

Exp ID	Estimated fO_2 (ΔIW)	Initial N content (ppm)	Measured N content (ppm)	F (remaining N fraction)	Measured $^{15}N/^{14}N$ ratios	Calculated $\delta^{15}N$ normalised (‰)	Bubbles present
V152-PB05N	0.0	910	798 ± 4	0.88 ± 0.01	0.871 ± 0.005	-79 ± 8	
V149-PB1N	-0.3	1945	1316 ± 16	0.68 ± 0.01	0.845 ± 0.028	-107 ± 34	
V129-PB2N	-1.0	5075	3084 ± 377	0.61 ± 0.07	0.916 ± 0.003	-32 ± 6	✓
V148-PB4N	-2.3	10435	4914 ± 102	0.47 ± 0.01	0.907 ± 0.011	-41 ± 13	✓
V133-PB4N2Si	-2.6	8371	8335 ± 194	1.00 ± 0.02	0.946 ± 0.003	0 ± 6	✓
V125-PB8N	-3.3	16076	13342 ± 841	0.83 ± 0.05	0.925 ± 0.004	-5 ± 7	✓
V151-PB6N3Si	-3.4	11353	7534 ± 526	0.66 ± 0.05	0.926 ± 0.007	-21 ± 10	✓
V150-PB8N6Si	-4.2	14609	13481 ± 735	0.93 ± 0.05	0.941 ± 0.006	-5 ± 9	✓

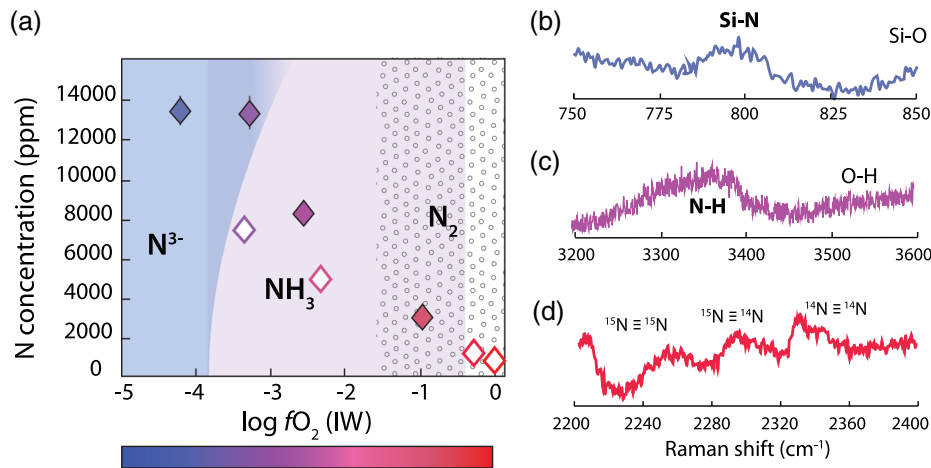


Figure 2 (a) N concentrations measured by SIMS in reduced glasses synthesised at variable fO_2 conditions, as represented by the colour scale. Open symbols represent samples that did not reach saturation. Raman spectra show (b) Si-N vibrations in sample V125-PB8N and also observed in sample V150-PB8N6Si, (c) N-H vibrations in sample V148-PB4N and also observed in all samples between IW-4 and IW-1 (pink shaded area in (a)), and (d) N_2 vibrations in sample V141-PB1N, corrected for air contamination, and also observed in samples V152-PB05N and V129-PB2N.

average). With increasing fraction of degassed N, $^{15}N/^{14}N$ ratios decreased from 0.946 ± 0.003 in the undegassed sample to 0.907 ± 0.011 in the most degassed sample (53 % of initial N lost). The $^{15}N/^{14}N$ ratios were normalised to the initial $^{15}N/^{14}N$ ratio of the undegassed glass V133-PB4N2Si (0.946 ± 0.003) and expressed as $\delta^{15}N_{norm}$ as:

$$\delta^{15}N_{norm} [‰] = \left[\left(\frac{^{15}N/^{14}N_{melt}}{^{15}N/^{14}N_{initial}} \right) - 1 \right] \cdot 1,000. \quad \text{Eq. 1}$$

These normalised values are not calculated relative to the atmospheric N isotopic composition ($^{15}N/^{14}N_{air} = 0.003676$) and cannot be directly compared to the $\delta^{15}N$ values of natural samples.

Degassing Models of N Isotopic Fractionation under Reduced Conditions

The normalised N isotopic composition of the glasses decreases from 0 ‰ in the undegassed glass to -41 ± 13 ‰ in the most degassed glass (Fig. 3). Although this $\delta^{15}N$ variation is opposite to that observed during MORB degassing (Cartigny *et al.*, 2001), it is consistent with glasses becoming isotopically lighter with increased degassing as observed for H, C, and S in natural settings (Supplementary Information). An open system degassing model, in which the exsolved vapour is immediately removed from contact with the melt during degassing, is suitable with the presence of gas bubbles within the dissolved forsterite rims (Fig. 1):

$$\delta^{15}N_{glass} = \delta^{15}N_{initial} + (F - 1)1,000 \ln \alpha, \quad \text{Eq. 2}$$

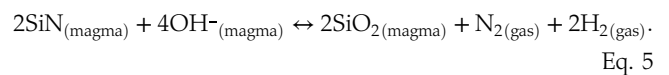
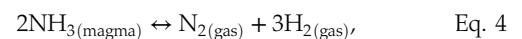
where $\delta^{15}N_{initial}$ is the “normalised initial” isotopic composition of the melt (here 0 ‰; sample V133-PB4N2Si), F is the fraction of N remaining in the melt, and α is the isotopic fractionation factor. In this case, open system degassing occurs in a finite N budget, conforming to a Rayleigh process (Equation 2).

In bubbles for which the gas pressure was sufficient to obtain a Raman signal above the noise, N was observed only as N_2 , even in very reduced samples in which N was dissolved as N-H complexes (V148-PB4N) and/or nitrides (V125-PB8N).

Therefore, we propose that at IW to IW-1, the N degassing reaction is:



Had the least reduced samples (V152-PB0.5N and V149-PB1N) not been affected by diffusion through cracks, they would be expected to degas following Equation 3, since N_2 is the only N species dissolved in those melts. In contrast, under more reduced conditions, N degassed as (*e.g.*, Dalou *et al.*, 2019a):



The fugacities of the relevant N species cannot be calculated at present due to a lack of thermodynamic data (see Supplementary Information).

To understand how N speciation can affect gas-melt N isotopic fractionation, we derived the basic equation for equilibrium isotopic fractionation for stable isotopes (Young *et al.*, 2015):

$$\Delta^{15}N_{gas-melt} = \frac{1,000}{24} \cdot \left(\frac{h}{k_b T} \right)^2 \left(\frac{\Delta m}{m_{14}m_{15}} \right) \times [(v_N^{gas^2} - v_N^{melt^2})(\mu_N^{gas} - \mu_N^{melt})], \quad \text{Eq. 6}$$

$$\alpha = \exp(\Delta^{15}N_{gas-melt}/1,000), \quad \text{Eq. 7}$$

where h is Planck’s constant ($J \cdot K^{-1}$), k_b is the Boltzmann constant ($J \cdot Hz^{-1}$), T is temperature (K), v^{gas} and v^{melt} denote the Raman vibration modes (Hz) of N species in the gas and silicate phases, respectively, and μ_N is the reduced mass of the N-bearing molecule. Using this expression, we calculated that the N isotopic fractionation factor at 1550 °C is 0.999 for degassing by Equation 3, and, under more reduced conditions, 1.005 for Equation 4, both in agreement with Hanschmann (1981), and 0.998 for Equation 5. These equilibrium fractionation factors cannot explain the variation of $\delta^{15}N_{norm}$ values observed in the degassed samples; the high isotopic fractionation undergone by these degassed melts rather suggests a kinetic process. Indeed, such large kinetic nitrogen isotopic effects have also



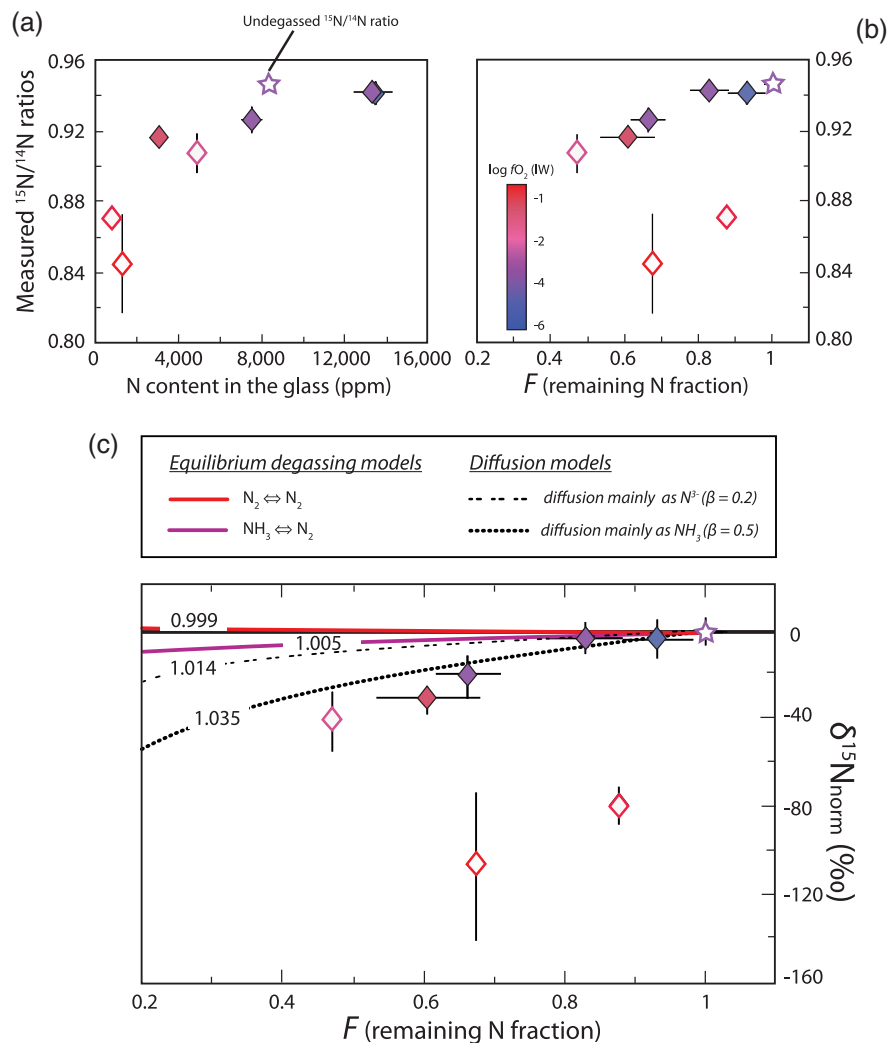


Figure 3 (a) $^{15}\text{N}/^{14}\text{N}$ ratios as a function of N content in glass, and (b) $^{15}\text{N}/^{14}\text{N}$ ratios, and (c) $\delta^{15}\text{N}$ values normalised to the initial value (see text) in reduced glasses as a function of F , the fraction of N remaining. F was calculated by dividing the measured N content in the glass by the estimated N content added to the starting material. Because all starting compositions were prepared from the same initial N-rich powder by variable mixes with a N-free powder, the initial $^{15}\text{N}/^{14}\text{N}$ ratios were the same in all starting materials. The degassing models are described in the text.

been observed in mantle-derived samples (Yokochi *et al.*, 2009). However, kinetic fractionation *via* evaporation results in increasingly heavy isotopic values (Saal and Hauri, 2021), opposite to our observations (Fig. 3c). The observed large isotopic fractionation may thus be explained by a variable diffusion process depending on N speciation, and therefore on $f\text{O}_2$ conditions. The magnitude of diffusive N isotopic fractionation during degassing is similar to that observed in natural high pressure-high temperature peridotitic systems (>25 ‰; Yokochi *et al.*, 2009; see Supplementary Information). Such a fractionation effect can be estimated from the ratio of the diffusion coefficients (D) of ^{14}N and ^{15}N , expressed as a function of their mass (m): $\frac{D_{^{14}\text{N}}}{D_{^{15}\text{N}}} = \left(\frac{m_{^{15}\text{N}}}{m_{^{14}\text{N}}}\right)^\beta$, where β is an empirical parameter with values between 0 and 0.5 that positively correlates with the diffusivity of the ion in silicate melts (Van Orman and Krawczynski, 2015). Hence, N_2 and NH_3 , which diffuse rapidly through silicate melts relative to Si, have a large isotopic effect (high β), whereas N^{3-} , which is bonded to Si, diffuses slowly (Boulliung *et al.*, 2021) and has a smaller isotopic effect (low β). Good fits to our data are $\beta = 0.2$ for N diffusing as N^{3-} and $\beta = 0.5$ for N as NH_3 (Fig. 3c). A simple diffusion process cannot explain the extremely large fractionation in undegassed samples (V152-PB0.5N and V149-PB1N), unless the diffusion of ^{14}N and ^{15}N is decoupled,

with ^{15}N favouring the stiffest bonds (N_2) and diffusing significantly faster than ^{14}N , favouring weaker N-H bonds in NH_3 . It is possible that N_2 diffusion in these melts is faster than degassing and controls the isotopic fractionation mechanism in these undegassed samples.

Evolution of the N Composition of Earth's Primitive Atmosphere

Figure 3 shows that $f\text{O}_2$ conditions determine N solubility and, therefore, the fraction of N degassed and the isotopic fractionation trends. Our results suggest that the upper layer of Earth's magma ocean degassed N as N_2 , regardless of $f\text{O}_2$ conditions, but that the intensity of N_2 degassing increased as the magma ocean became less reduced. This is in agreement with the recent model of Sossi *et al.* (2020), which predicts that Earth's prebiotic atmosphere was dominated by CO_2 and N_2 gases.

Whether N was dissolved in the magma ocean as nitride, ammonia, or both, N loss depleted the surface or upper parts of the magma ocean in ^{15}N relative to the atmosphere. This could have produced the currently observed isotopic differences between the ^{15}N -depleted mantle ($\delta^{15}\text{N} = -5 \pm 2$ ‰ in diamonds and MORBs) and the ^{15}N -enriched surface ($\delta^{15}\text{N} = +6$ ‰ in

sediments and $\delta^{15}\text{N} = 0$ ‰, by definition, in the atmosphere) (Cartigny and Marty, 2013). Other explanations of the N isotopic distribution among terrestrial reservoirs include *i*) recycling (subduction) of surficial materials, and *ii*) core–mantle differentiation (Li *et al.*, 2016; Dalou *et al.*, 2019b) However, Labidi *et al.* (2020) recently showed that N recycling is inefficient. How core–mantle differentiation would have affected the upper layer of the magma ocean and thus the present day depleted mantle, would have depended on the depth of the magma ocean and the efficiency of post-magma ocean convection to homogenise the $\delta^{15}\text{N}$ value of the mantle; thus this process remains disputable.

Acknowledgements

We thank Johan Villeneuve for his assistance and support during SIMS analyses, Jean-Luc Devidal for performing microprobe analyses on silicate glasses, and Marie-Camille Caumon for her help with Raman spectroscopy analyses. We are grateful to Robert Dennen for English editing. We thank reviewers Paolo Sossi and Sami Mikhail for their comments that greatly improved the manuscript, and editor Helen Williams for handling the manuscript. This work was supported by the European Research Council under the European Union's Horizon 2020 research and innovation program (Grant Agreement no. 715028). This is CRPG contribution 2812.

Editor: Helen Williams

Additional Information

Supplementary Information accompanies this letter at <https://www.geochemicalperspectivesletters.org/article2204>.



© 2022 The Authors. This work is distributed under the Creative Commons Attribution Non-Commercial No-Derivatives 4.0

License, which permits unrestricted distribution provided the original author and source are credited. The material may not be adapted (remixed, transformed or built upon) or used for commercial purposes without written permission from the author. Additional information is available at <https://www.geochemicalperspectivesletters.org/copyright-and-permissions>.

Cite this letter as: Dalou, C., Deligny, C., Füre, E. (2022) Nitrogen isotope fractionation during magma ocean degassing: tracing the composition of early Earth's atmosphere. *Geochem. Persp. Let.* 20, 27–31. <https://doi.org/10.7185/geochemlet.2204>

References

- BERNADOU, F., GAILLARD, F., FÜRI, E., MARROCCHI, Y., SŁODCZYK, A. (2021) Nitrogen solubility in basaltic silicate melt—Implications for degassing processes. *Chemical Geology* 573, 120192.
- BOULLIUNG, J., FÜRI, E., DALOU, C., TISSANDIER, L., ZIMMERMANN, L., MARROCCHI, Y. (2020) Oxygen fugacity and melt composition controls on nitrogen solubility in silicate melts. *Geochimica et Cosmochimica Acta* 284, 120–133.
- BOULLIUNG, J., DALOU, C., TISSANDIER, L., FÜRI, E., MARROCCHI, Y. (2021) Nitrogen diffusion in silicate melts under reducing conditions. *American Mineralogist* 106, 662–666.
- CARTIGNY, P., MARTY, B. (2013) Nitrogen isotopes and mantle geodynamics: The emergence of life and the atmosphere–crust–mantle connection. *Elements* 9, 359–366.
- CARTIGNY, P., JENDRZEJEWSKI, N., PINEAU, F., PETIT, E., JAVOY, M. (2001) Volatile (C, N, Ar) variability in MORB and the respective roles of mantle source heterogeneity and degassing: the case of the Southwest Indian Ridge. *Earth and Planetary Science Letters* 194, 241–257.
- DALOU, C., HIRSCHMANN, M.M., JACOBSEN, S.D., LE LOSQ, C. (2019a) Raman spectroscopy study of C–O–H–N speciation in reduced basaltic glasses: Implications for reduced planetary mantles. *Geochimica et Cosmochimica Acta* 265, 32–47.
- DALOU, C., FÜRI, E., DELIGNY, C., PIANI, L., CAUMON, M.C., LAUMONIER, M., BOULLIUNG, J., EDÉN, M. (2019b) Redox control on nitrogen isotope fractionation during planetary core formation. *Proceedings of the National Academy of Sciences* 116, 14485–14494.
- ELKINS-TANTON, L.T. (2012) Magma oceans in the inner solar system. *Annual Review of Earth and Planetary Sciences* 40, 113–139.
- FROST, D.J., MANN, U., ASAHARA, Y., RUBIE, D.C. (2008) The redox state of the mantle during and just after core formation. *Philosophical Transactions of the Royal Society A: Mathematical, Physical and Engineering Sciences* 366, 4315–4337.
- GAILLARD, F., BOUHIFD, M.A., FÜRI, E., MALAVERGNE, V., MARROCCHI, Y., NOACK, L., ORTENZI, G., ROSKOSZ, M., VULPIUS, S. (2021) The Diverse Planetary Ingressing/Outgassing Paths Produced over Billions of Years of Magmatic Activity. *Space Science Reviews* 217, 1–54.
- GOLDBLATT, C., CLAIRE, M.W., LENTON, T.M., MATTHEWS, A.J., WATSON, A.J., ZAHNLE, K.J. (2009) Nitrogen-enhanced greenhouse warming on early Earth. *Nature Geosciences* 2, 891–896.
- GREWAL, D.S., DASGUPTA, R., FARNELL, A. (2020) The speciation of carbon, nitrogen, and water in magma oceans and its effect on volatile partitioning between major reservoirs of the Solar System rocky bodies. *Geochimica et Cosmochimica Acta* 280, 281–301.
- HANSCHMANN, G. (1981) Quantum chemical calculations of isotope effects in nitrogen-containing molecules. *ZfI-Mitteilungen* 41, 19–39.
- JAVOY, M., PINEAU, F., DELORME, H. (1986) Carbon and nitrogen isotopes in the mantle. *Chemical Geology* 57, 41–62.
- KASTING, J.F. (1993) Earth's early atmosphere. *Science* 259, 920–926.
- LABIDI, J., BARRY, P.H., BEKAERT, D.V., BROADLEY, M.W., MARTY, B., GIUNTA, T., WARR, O., SHERWOOD LOLLAR, B., FISHER, T.B., AVICE, G., CARACAUSI, A., BALLENTINE, C.J., HALDARSSON, S.A., STEFANSSON, A., KURZ, M.D., KOHL, I.E., YOUNG, E.D. (2020) Hydrothermal ^{15}N abundances constrain the origins of mantle nitrogen. *Nature* 580, 367–371.
- LI, Y., KEPPLER, H. (2014) Nitrogen speciation in mantle and crustal fluids. *Geochimica et Cosmochimica Acta* 129, 13–32.
- LI, Y.F., MARTY, B., SHCHEKA, S., ZIMMERMANN, L., KEPPLER, H. (2016) Nitrogen isotope fractionation during terrestrial core–mantle separation. *Geochemical Perspectives Letters* 2, 138–147.
- LIBOUREL, G., MARTY, B., HUMBERT, F. (2003) Nitrogen solubility in basaltic melt. Part I. Effect of oxygen fugacity. *Geochimica et Cosmochimica Acta* 67, 4123–4135.
- MARTY, B., DAUPHAS, N. (2003) The nitrogen record of crust–mantle interaction and mantle convection from Archean to present. *Earth and Planetary Sciences Letters* 206, 397–410.
- MIKHAIL, S., SVERJENSKY, D.A. (2014) Nitrogen speciation in upper mantle fluids and the origin of Earth's nitrogen-rich atmosphere. *Nature Geosciences* 7, 816–819.
- MOSENFELDER, J.L., VON DER HANDT, A., FÜRI, E., DALOU, C., HERVIG, R.L., ROSSMAN, G.R., HIRSCHMANN, M.M. (2019) Nitrogen incorporation in silicates and metals: Results from SIMS, EPMA, FTIR, and laser-extraction mass spectrometry. *American Mineralogist* 104, 31–46.
- VAN ORMAN, J.A., KRAWCZYNSKI, M.J. (2015) Theoretical constraints on the isotope effect for diffusion in minerals. *Geochimica et Cosmochimica Acta* 164, 365–381.
- SAAL, A.E., HAURI, E.H. (2021) Large sulfur isotope fractionation in lunar volcanic glasses reveals the magmatic differentiation and degassing of the Moon. *Science Advances* 7, eabe4641.
- SOSSI, P.A., BURNHAM, A.D., BADRO, J., LANZIROTTI, A., NEWVILLE, M., O'NEILL, H.S.C. (2020) Redox state of Earth's magma ocean and its Venus-like early atmosphere. *Science Advances* 6, eabd1387.
- YOKOCHI, R., MARTY, B., CHAZOT, G., BURNARD, P. (2009) Nitrogen in peridotite xenoliths: Lithophile behavior and magmatic isotope fractionation. *Geochimica et Cosmochimica Acta* 73, 4843–4861.
- YOUNG, E.D., MANNING, C.E., SCHAUBLE, E.A., SHAHAR, A., MACRIS, C.A., LAZAR, C., JORDAN, M. (2015) High-temperature equilibrium isotope fractionation of non-traditional stable isotopes: Experiments, theory, and applications. *Chemical Geology* 395, 176–195.
- ZAHNLE, K.J., LUPU, R., CATLING, D.C., WOGAN, N. (2020) Creation and evolution of impact-generated reduced atmospheres of early Earth. *Planetary Science Journal* 1, 11.



Nitrogen isotope fractionation during magma ocean degassing: tracing the composition of early Earth's atmosphere

C. Dalou, C. Deligny, E. Füre

Supplementary Information

The Supplementary Information includes:

- 1. Methods
- 2. Supplementary Discussion
- Tables S-1 and S-2
- Figures S-1 to S-3
- Supplementary Information References

1. Methods

Synthesis of starting material

Two series of mafic glasses were prepared:

- a series of Fe-free glasses, noted PB, for the degassing experiments presented in the main text was designed to equilibrate magma-ocean-like melts with a N-rich gas; and to avoid N partitioning into Fe metal blobs at low fO_2 conditions (Dalou *et al.*, 2017; Speelmanns *et al.*, 2019; Grewal *et al.*, 2019).
- a series of Fe-bearing glasses, noted PBF, was designed to equilibrate magma-ocean-like melts and a Fe-N or Fe-Si-N alloy (\pm N-rich gas) under reducing conditions to allow the calculation of fO_2 conditions.

These mafic glasses were synthesised based on the magma ocean composition proposed by Fichtner *et al.* (2021). The starting composition was chosen to account for MgO dissolution from the forsterite capsule at 1550 °C, which here increased the MgO concentration of the melt from 9.7 to up to 22 wt. % (Table S-1). Using this composition, we obtained well-quenched MgO-rich glasses that were relatively depolymerised (*i.e.* NBO/T \geq 1, where NBO/T is the ratio of non-bridging oxygens to tetrahedral cations).

The starting powders were prepared by mixing pre-dried, spectroscopically pure SiO₂, Al₂O₃, MgO, CaCO₃, Na₂CO₃, and K₂CO₃ reagents. The mixtures were decarbonated by slow heating (3 °C/min), then fused in air for 2 h at 1350 °C in platinum crucibles in a 1 atm furnace. Melts were quenched to glass in water, then crushed and hand ground



in an agate mortar for 45 min. After decarbonating the glass powders, Fe was added to the PBF series as FeO powder, whereas the PB series remained Fe free. Nitrogen was added to both series using 0.5–8 wt. % Si_3N_4 , noted ‘0.5N’ to ‘8N’ in the sample names. Both $\text{Si}_3^{14}\text{N}_4$ and $\text{Si}_3^{15}\text{N}_4$ powders (prepared as described in Dalou *et al.*, 2019) were used to yield an initial $^{15}\text{N}/^{14}\text{N}$ ratio of 0.946 ± 0.003 . By varying the amount of Si_3N_4 added to the starting compositions and adding additional Si powder (2, 3 and 6 wt. %, noted ‘2Si’, ‘3Si’, and ‘6Si’ in the sample names), we were able to change (but not control) the sample $f\text{O}_2$ because Si_3N_4 and Si have a strong reducing effect (Dalou *et al.*, 2017). The starting materials were loaded into pure forsterite capsules to ensure reducing conditions and prevent N loss. Glasses were originally anhydrous but were likely contaminated by atmospheric hydrogen, since N-H vibrations were observed in the experimental run products.

Experimental procedure

Experiments were performed in a 1/2-inch piston cylinder at 1.5 GPa and 1550 °C at the Centre de Recherches Pétrographiques et Géochimiques (CRPG, Nancy, France). Run temperatures were controlled to within ~ 1 °C of the set point using $\text{W}_{95}\text{Re}_5/\text{W}_{74}\text{Re}_{26}$ thermocouples. The duration of the experiments was 6 h, which is sufficient to reach compositional equilibrium (Dalou *et al.*, 2017). Before decompression, the power to the furnace was cut and the experiment was quenched rapidly (~ 175 °C/s). During this stage of decompression, the forsterite capsules suffered cracking, which divided them into three to six lamellae 0.2–0.8 mm thick.

Hence, the final run product from each experiment consisted of various lamellae of glass embedded in forsterite, which were individually mounted in epoxy and polished with ethanol. For each experiment, the best sample was selected: the sample with the largest bubbles was selected for Raman spectroscopy (PB series) and that with the largest metal blobs for electron probe microanalysis (EPMA, all glasses). The selected lamellae were then removed from the resin, pressed into high-purity indium metal mounts, and gold coated for SIMS analysis. After re-polishing to remove any coating to avoid interference from Au vibrational bands, mounts from the PB series were analysed by Raman spectroscopy, and then all glasses were carbon coated for EPMA.

SIMS analyses

In-situ SIMS analyses of N concentrations and isotopic ratios in the silicate glasses were performed at the CRPG using the CAMECA 1280-HR2. Nitrogen ($^{14}\text{N} + ^{15}\text{N}$) contents and isotopic ratios (Table 1) were measured by analysing the secondary molecular ions $^{14}\text{N}^{16}\text{O}^-$ and $^{15}\text{N}^{16}\text{O}^-$ at masses 30 and 31, respectively, at a nominal mass resolution of 14,000. A 10 kV Cs^+ primary ion beam was used with a ~ 10 nA current, resulting in a beam diameter of 15–20 μm , and a normal-incidence electron gun was used for charge compensation. To minimise surface contamination, glass surfaces were pre-sputtered for 180 s over a 10×10 μm area prior to signal acquisition. Further details on the SIMS N analysis procedure are available in Füre *et al.* (2018). The $^{14}\text{N}^{16}\text{O}^-$ and $^{15}\text{N}^{16}\text{O}^-$ ions were measured for 30 cycles in peak-jumping mode on an electron multiplier for 6 s, together with $^{27}\text{Al}^-$ (3 s), $^{30}\text{Si}^-$ (3 s), and $^{16}\text{O}_2^-$ (3 s) on a faraday cup. We used a suite of eight reference glasses with known N concentrations and isotopic compositions to determine the N contents in



the silicate glasses based on the $^{14}\text{N}^{16}\text{O}^-$ count rate normalised by the $^{16}\text{O}_2^-$ signal (Füri *et al.*, 2018). This method has been shown to yield N contents in excellent agreement with static mass spectrometry analyses for glasses of variable composition and containing ≤ 1 to 6,000 ppm N (Boulliung *et al.*, 2020). Based on repeated isotopic ratio measurements of five reference glasses containing ≥ 136 ppm N ($\delta^{15}\text{N}_{\text{true}} = -4 \pm 1 \text{ ‰}$), the instrumental mass fractionation (IMF) for glass analyses was determined to be $\alpha_{\text{inst}} = 1.0120 \pm 0.0015$ (2σ ; Fig. S-1). Thus, the measured $^{15}\text{N}/^{14}\text{N}$ ratios of the experimental glasses were corrected for IMF as $(^{15}\text{N}/^{14}\text{N})_{\text{corr}} = (^{15}\text{N}/^{14}\text{N})_{\text{measured}} / \alpha_{\text{inst}}$.

Raman spectroscopy analyses

Raman spectroscopy was performed using a LabRAM HR microspectrometer (Horiba Jobin Yvon) at GeoRessources (Nancy, France) using the 457.9 nm radiations of an Ar^+ laser (Stabilite 2017, Spectra-Physics) with 154 mW output. The laser intensity was focused to a $\sim 2 \mu\text{m}$ spot-size with 7 mW on-sample through a $50\times$ long-working-distance Olympus objective with a 0.5 numerical aperture. The spectrometer was equipped with a 1,800 grooves/mm grating. Acquisition times were 10 s, with 20 acquisitions collected per spectrum. To observe Si-N vibrations, molecular N_2 vibrations, and N-H vibrations in the degassed silicate glasses, spectra were acquired in the 700–1200, 2000–2400, and 3060–3560 cm^{-1} spectral windows, respectively. No baseline corrections were applied to the spectra presented in Figure 3.

To analyse gas bubble contents, the laser was focused into the largest bubbles ($>30 \mu\text{m}$ in diameter) and spectra were acquired for 15 s with 30 acquisitions, centred on the 2200 and 3160 cm^{-1} spectral windows. In these bubbles, the N triple bond vibration of molecular N_2 , and the C-H vibration in CH_4 were observed at 2331 and 2917 cm^{-1} , respectively (Fig. S-2). We note the absence of N-H vibrations in the range 3200–3450 cm^{-1} .

EPMA

Major element compositions of glasses and metal blobs (in Fe-bearing samples) were determined using a CAMECA SXFive-Tactics at the Laboratoire Magmas et Volcans (Clermont-Ferrand, France). For glass analyses, we used an accelerating voltage of 15 kV and a 8 nA beam defocused to 10 μm . Wollastonite (Si, Ca), basaltic glass VG2 (Al), Fe_2O_3 (Fe), MgO (Mg), and albite (Na) were used as standards. For metal alloys, we used a 15 kV accelerating voltage and a 15 nA focused beam. Along with Fe, the Pt and Si concentrations in the metal phases of all samples were measured, and pure Fe, Si, and Pt were used as metal standards. Aluminium was analysed to check for silicate contamination during metal analyses, using VG2 as a standard. The major element compositions of silicate glasses determined by EPMA are presented in Table S-1 and those of metal blobs in Table S-2.



Oxygen fugacity calculation

Oxygen fugacities, expressed as $\log f_{\text{O}_2}$ (IW), were estimated from the equilibrium reaction $\text{FeO}_{\text{silicate melt}} = \text{Fe}_{\text{liquid metal}} + 1/2 \text{O}_2$ for Fe-bearing samples. Following this equilibrium, f_{O_2} was calculated using the relationship between the mole fractions of FeO in silicate melt ($X_{\text{FeO}}^{\text{melt}}$) and Fe in liquid metal ($X_{\text{Fe}}^{\text{alloy}}$), their associated activity coefficients ($\gamma_{\text{FeO}}^{\text{melt}}$ and $\gamma_{\text{Fe}}^{\text{alloy}}$, respectively), and the equilibrium constant (K) of the reaction (Médard *et al.*, 2008) as described in Dalou *et al.* (2017):

$$\log_{10} f_{\text{O}_2} = \frac{2}{\ln(10)} \left[\ln \left(\frac{X_{\text{FeO}}^{\text{melt}}}{X_{\text{Fe}}^{\text{alloy}}} \right) - \ln \left(\gamma_{\text{Fe}}^{\text{alloy}} \right) + \ln \left(\gamma_{\text{FeO}}^{\text{melt}} \right) - \ln K \right] \quad \text{Eq. S-1}$$

$\gamma_{\text{Fe}}^{\text{alloy}}$ was derived via the MetalAct metal activity calculator (Wade and Wood, 2005) for each sample and $\gamma_{\text{FeO}}^{\text{melt}}$ was assumed to be 1.2 (Dalou *et al.*, 2017, 2019). We used the method of Stanley *et al.* (2014) and Zhang *et al.* (2016) to directly compare the resulting f_{O_2} to the IW buffer, which is referenced to solid Fe metal. The f_{O_2} conditions of the PBF series could only be determined in 5 samples (Fig. S-3a and Table S-2), in which the metal blobs were $>5 \mu\text{m}$ in diameter (Fig. S-3b); the f_{O_2} values of these samples range from IW -2.3 to IW -4.2 . The f_{O_2} conditions in samples PBF05N and PBF2N, in which metal blobs were too small to be analysed, were roughly estimated by extrapolation of the trend in Figure S-3a.

Because each PB sample has an equivalent PBF sample in terms of initial Si_3N_4 and Si metal concentrations (*e.g.*, PB4N2Si and PBF4N2Si), we assumed that the f_{O_2} determined for each PBF sample corresponds to that of its equivalent in the PB series. Although this is a very rough approximation (± 0.5 log units), this indirect method of estimating f_{O_2} in the degassed Fe-free glasses enabled us to discuss the effect of f_{O_2} conditions on N solubility in the main text.

$P(\text{N}_2)$ calculation

Determining the partial pressure of nitrogen $P(\text{N}_2)$ or nitrogen fugacity f_{N_2} in the gas phase (*i.e.*, bubbles) of the samples from this study could provide more quantitative information on the effect of the gas composition on the solubility and isotopic fractionation of N. Indeed, it could be used to calculate the equilibrium constant K of the different N degassing reactions. Bernadou *et al.* (2021) calculated $P(\text{N}_2)$ in the fluid phase of their experiments by quantifying the partial pressure of other species within the fluid phase: H_2O , CO_2 , CO, and H_2 . They determined the pressure of H_2O and CO_2 by converting the measured IR band intensities into concentrations following Shishkina *et al.* (2010), and then into partial pressures using the numerical model of Iacono-Marziano *et al.* (2012). The partial pressures of CO and H_2 were determined using the activities of C (graphite) and water and f_{O_2} by using the equilibrium reaction presented in Bernadou *et al.* (2021). They then calculated $P(\text{N}_2)$ by subtracting the fugacities of the other species from the “total



pressure” of the experiment and converted $P(\text{N}_2)$ to $f\text{N}_2$ by applying different coefficients depending on the pressure conditions of their experiments.

Unfortunately, we cannot apply this method to our experiments because only two bubbles in two experiments performed at the same pressure and temperature conditions were analysed by Raman spectroscopy. As previously mentioned, N_2 and CH_4 were detected in the bubbles by Raman spectroscopy, but, unlike IR band intensities, Raman band intensities cannot be converted into concentrations, which are necessary to follow the methods of [Bernadou *et al.* \(2021\)](#) or [Hirschmann *et al.* \(2012\)](#) for H_2 . Moreover, because N_2 is not the only gas species in the bubbles, its pressure cannot be considered as equivalent to the confining pressure. Even considering the mixed gases species in the bubbles, [Zhang and Duan \(2009\)](#) do not provide the equations of state to calculate the fugacities of N_2 and CH_4 at pressure conditions relevant to our study (>1 GPa). Therefore, calculating $P(\text{N}_2)$ in the samples from this study would require numerous assumptions and generate meaningless values.

2. Supplementary Discussion

H, C, and S isotopic variations observed during basaltic magma degassing

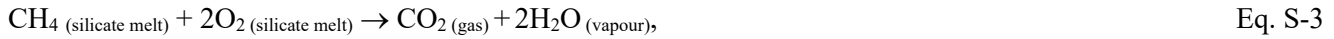
Studies of degassed basalts, whether terrestrial mid-ocean ridge basalts ([Pineau and Javoy, 1994](#); [Cartigny *et al.*, 2001](#)), ocean island basalts ([Gerlach and Taylor, 1990](#); [Aubaud *et al.*, 2006](#)), arc basalts ([De Hoog *et al.*, 2001](#); [Hauri, 2002](#)), or lunar basalts ([Saal and Hauri, 2021](#)) have shown H, C, and S isotopic variations consistent with our observations for N isotopes during degassing.

In natural degassed basaltic glasses, H and C become isotopically lighter with increased degassing (*e.g.*, [Taylor *et al.*, 1986](#); [Gerlach and Taylor, 1990](#); [Pineau and Javoy, 1994](#); [Cartigny *et al.*, 2001](#); [Hauri, 2002](#)). For instance, melt inclusions from a single Hawaiian volcano display δD values from -61 ± 4 ‰ to -165 ± 4 ‰ ([Hauri, 2002](#)). Whereas the heavier δD values (> -70 ‰) can be explained by a kinetic isotopic fractionation due to H diffusion from the melt inclusions, the most negative values (-103 ± 4 ‰ to -165 ± 4 ‰) negatively correlate with their water contents. This variation of δD values was modelled by the shallow open-system degassing of H_2O vapour with a vapour-melt hydrogen isotopic fractionation factor of 1.024 ([Hauri, 2002](#)). Thus, increased equilibrium degassing of H produces isotopically lighter silicate melts. This applies for the degassing of H as H_2O under present-day volcanic degassing conditions. Under more reduced conditions, such a lunar or martian magmatic degassing, H degasses as H_2 or CH_4 , producing isotopically heavier silicate melts as degassing increases ([Taylor *et al.*, 1986](#)).

Evidently, the degrees of such fractionations are expected to be smaller for C and S than for H due to the smaller relative mass differences between their isotopes. However, large C isotopic fractionations produced by C degassing have also been observed in degassed MORBs. For instance, $\delta^{13}\text{C}$ values range between -11.4 and -4.3 ‰ in MORBs from the South Indian Ridge and positively correlate with sample vesicularity, confirming the influence of degassing on C isotopic fractionation ([Cartigny *et al.*, 2001](#)). In melt inclusions from Koolau volcano, Hawaii, [Hauri \(2002\)](#) also observed large $\delta^{13}\text{C}$ variations (-12 to -21 ‰), again explained by C degassing. In both cases, these wide ranges of $\delta^{13}\text{C}$



values were explained by open-system (Rayleigh) rather than closed-system degassing. Yet, in the South Indian Ridge MORBs, the observed N isotopic fractionation during degassing is opposite to that of C isotopes, *i.e.* $\delta^{15}\text{N}$ values increase from -5.9 to $+2.1$ ‰ in the residual melt with increased degassing (Cartigny *et al.*, 2001). The opposite fractionation trends of C and N isotopes during degassing can be explained by their equilibrium degassing reactions. Carbon degasses as:



depending on whether it dissolves as carbonate or its more reduced form. Both degassing reactions produce a gas-melt isotopic fractionation factor >1 as determined by Javoy *et al.* (1976), and thus isotopically lighter silicate melts with increased C degassing. In contrast, in MORBs and OIBs, N is dissolved under its molecular form and degasses as:



which, as modelled in Figure 3, produces a gas-melt isotopic fractionation factor of 0.999, and thus isotopically heavier silicate melts with increased degassing. Under the more reduced conditions investigated in this study to simulate magma ocean degassing, this N degassing reaction no longer holds, as shown by Equations 4 and 5.

Sulfur degassing is more complex because sulfur is dissolved and degassed as multiple gaseous species depending on $f\text{O}_2$ conditions. Under reducing conditions comparable to those investigated herein, S dissolves into silicate melts as S^{2-} (Jugo *et al.*, 2010) and can degas as H_2S , COS , and S_2 in various proportions depending on pressure, temperature, and $f\text{O}_2$ conditions (Renggli *et al.*, 2017). Simplifying the issue by taking an average gas-melt sulfur isotopic fractionation factor of 1.003, Saal and Hauri (2021) successfully modelled the large variation of $\delta^{34}\text{S}$ values measured in lunar volcanic glasses ($+1.3$ to -14 ‰) as equilibrium open-system degassing. Therefore, increased degassing of sulfur under reduced conditions decreases the $\delta^{34}\text{S}$ values of silicate melts. However, at higher $f\text{O}_2$ conditions, S is dissolved as SO_4^{2-} in the silicate melt and degasses either as SO_2 or H_2S , and the $\delta^{34}\text{S}$ values of the silicate melt increase with increasing degassing (de Moor *et al.*, 2013).

Large kinetic nitrogen isotopic effects observed in natural mantle samples

Large variations have been observed among the nitrogen isotopic compositions of diverse mantle samples including diamonds (*e.g.*, Mikhail *et al.*, 2014) and xenoliths (Yokochi *et al.*, 2009; Banerjee *et al.* 2015; Yamamoto *et al.*, 2020). For instance, Yokochi *et al.* (2009) reported large isotopic disequilibria up to 25.4 ‰ between ferromagnesian minerals (olivine and pyroxene with positive $\delta^{15}\text{N}$ values) and phlogopite (with $\delta^{15}\text{N}$ as low as -17.3 ‰) in single peridotite xenoliths. Furthermore, both peridotitic and eclogitic diamonds show $\delta^{15}\text{N}$ values varying from <-40 ‰ to $>+20$ ‰ (Mikhail *et al.*, 2014). Whereas some of these variations can be explained by source variability, others cannot,



particularly $\delta^{15}\text{N}$ heterogeneities observed in single diamond samples (≤ 33 ‰; Mikhail *et al.*, 2014). Very interestingly, $\delta^{15}\text{N}$ variations in both xenoliths and diamonds are of the same order of magnitude as those measured in the degassed glasses from this study and are, therefore, too large to be explained by equilibrium N isotopic fractionations. Whereas Mikhail *et al.* (2014) could not conclude with certainty that kinetic isotopic fractionation was the only cause for the large range of $\delta^{15}\text{N}$ values they measured, Yokochi *et al.* (2009) presented evidence for kinetic isotopic fractionation during the substitution of NH_4^+ for N_2 in phlogopite during N uptake from the host magma. Therefore, as discussed in the main text, large kinetic N isotopic fractionations (≥ 25 ‰) resulting from a diffusive process at magmatic temperatures can be observed in natural settings and reproduced experimentally at high pressure and high temperature.

Supplementary Tables

Table S-1 Major element contents (wt. %) of silicate glasses; bdl, below detection limit.

Exp ID	SiO ₂	Al ₂ O ₃	FeO	MgO	CaO	Na ₂ O	K ₂ O	Total
<i>Fe-free degassed glasses</i>								
V152-PB05N	52.9 ± 0.3	7.8 ± 0.1	bdl	19.9 ± 0.3	6.8 ± 0.1	7.7 ± 0.1	3.4 ± 0.1	98.4 ± 0.3
V149-PB1N	52.5 ± 0.2	7.8 ± 0.2	bdl	20.5 ± 0.4	7.1 ± 0.1	7.2 ± 0.1	3.3 ± 0.1	98.3 ± 0.3
V129-PB2N	53.0 ± 0.2	7.9 ± 0.1	bdl	20.0 ± 0.4	6.7 ± 0.1	7.6 ± 0.1	3.5 ± 0.1	98.6 ± 0.4
V148-PB4N	54.2 ± 0.2	7.0 ± 0.1	bdl	21.3 ± 0.3	6.6 ± 0.2	7.2 ± 0.1	3.1 ± 0.1	99.3 ± 0.5
V133-PB4N2Si	57.9 ± 0.3	8.7 ± 0.1	bdl	17.0 ± 0.1	6.2 ± 0.1	7.6 ± 0.1	3.4 ± 0.1	100.8 ± 0.5
V125-PB8N	52.2 ± 0.2	7.4 ± 0.1	bdl	19.7 ± 0.2	6.6 ± 0.1	7.2 ± 0.1	3.1 ± 0.1	101.2 ± 0.2
V151-PB6N3Si	58.1 ± 0.4	6.3 ± 0.1	bdl	21.9 ± 0.3	5.5 ± 0.1	6.3 ± 0.1	2.6 ± 0.1	99.7 ± 0.3
V150-PB8N6Si	61.6 ± 0.6	5.7 ± 0.2	bdl	19.8 ± 0.6	6.0 ± 0.1	5.5 ± 0.1	2.6 ± 0.1	101.2 ± 0.4
<i>Fe-bearing glasses</i>								
V153-PBF05N	47.2 ± 0.3	8.3 ± 0.2	2.8 ± 0.1	19.6 ± 0.6	6.8 ± 0.1	7.5 ± 0.2	3.4 ± 0.1	95.7 ± 0.4
V142-PBF2N	50.2 ± 0.4	7.7 ± 0.1	4.5 ± 0.1	18.4 ± 0.2	7.1 ± 0.1	7.3 ± 0.1	3.4 ± 0.1	98.7 ± 0.4
V141-PBF4N	50.9 ± 0.3	8.0 ± 0.1	2.0 ± 0.1	18.6 ± 0.3	7.5 ± 0.1	6.5 ± 0.1	3.3 ± 0.1	96.7 ± 0.4
V145-PBF4N2Si	53.4 ± 0.2	7.2 ± 0.1	1.8 ± 0.1	19.6 ± 0.4	6.4 ± 0.1	6.5 ± 0.1	3.2 ± 0.1	98.1 ± 0.5
V147-PBF8N	54.9 ± 0.4	7.0 ± 0.2	0.9 ± 0.1	20.2 ± 0.4	6.2 ± 0.1	7.0 ± 0.2	3.2 ± 0.1	99.3 ± 0.4
V154-PBF6N3Si	58.0 ± 0.5	6.9 ± 0.1	0.8 ± 0.4	19.4 ± 0.3	5.9 ± 0.1	6.3 ± 0.1	3.0 ± 0.1	100.3 ± 0.5
V155-PBF8N6Si	62.8 ± 0.5	5.9 ± 0.2	0.2 ± 0.2	19.6 ± 0.3	5.0 ± 0.1	5.5 ± 0.1	2.7 ± 0.1	101.6 ± 0.7



Table S-2 Fe, Pt, and Si contents (wt. %) of metal blobs and estimated fO_2 conditions.

Exp ID	Fe	Pt	Si	fO_2 (IW)
V141- PBF4N	92.0 ± 0.3	0.03 ± 0.03	0.04 ± 0.02	−2.3
V145-PBF4N2Si	94.0 ± 0.2	0.16 ± 0.04	0.007 ± 0.004	−2.6
V147-PBF8N	94.2 ± 0.4	0.30 ± 0.06	0.04 ± 0.01	−3.3
V154-PBF6N3Si	92.9 ± 0.3	0.4 ± 0.2	0.007 ± 0.002	−3.4
V155-PBF8N6Si	77.1 ± 0.9	1.8 ± 1.8	20.9 ± 1.1	−4.2

Supplementary Figures

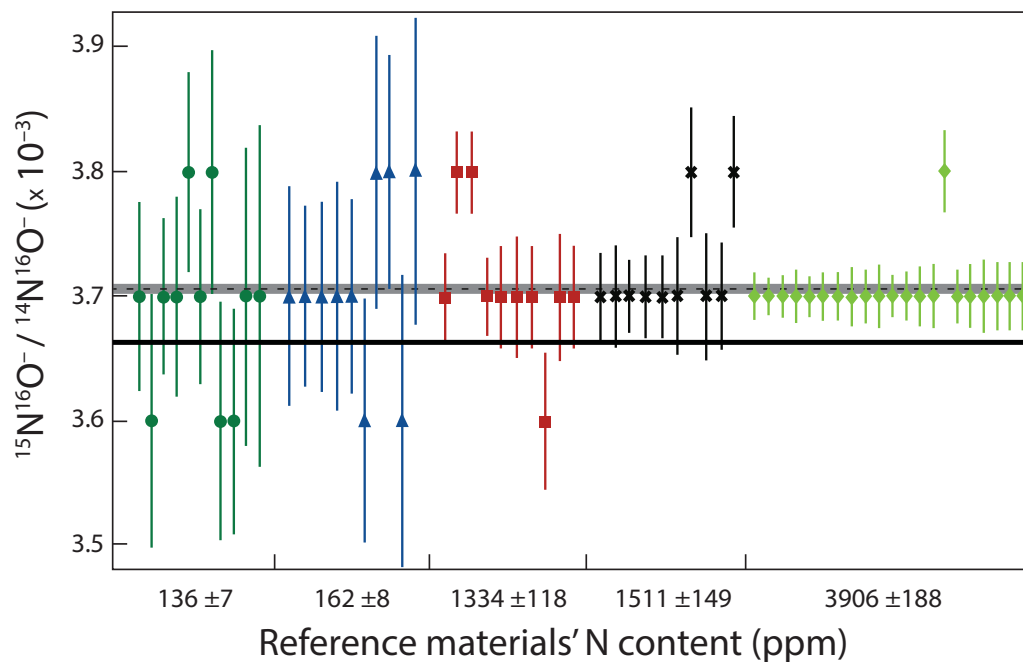


Figure S-1 Measured $^{15}N^{16}O^- / ^{14}N^{16}O^-$ ratios in five reference glasses used to calculate IMF. Each symbol corresponds to a reference glass whose N content was previously measured by static mass spectrometry (Füri *et al.*, 2018). The dashed line is the average of all standard analyses calculated using IsoplotR (Vermeesch, 2018) with 2σ uncertainties (shown by the grey shaded bar). The true $^{15}N/^{14}N$ value of these reference glasses is shown by the black line (~ 0.003662). The ratio of the average to the true value (*i.e.* the dashed and solid lines, respectively) is α_{inst} .

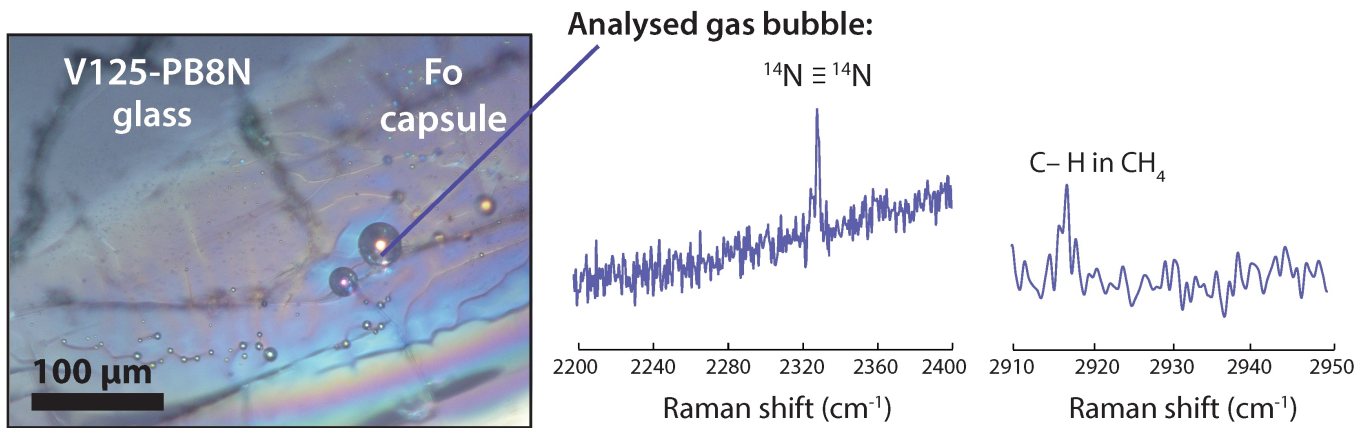


Figure S-2 Raman spectra obtained in bubbles of sample V125-PB8N.

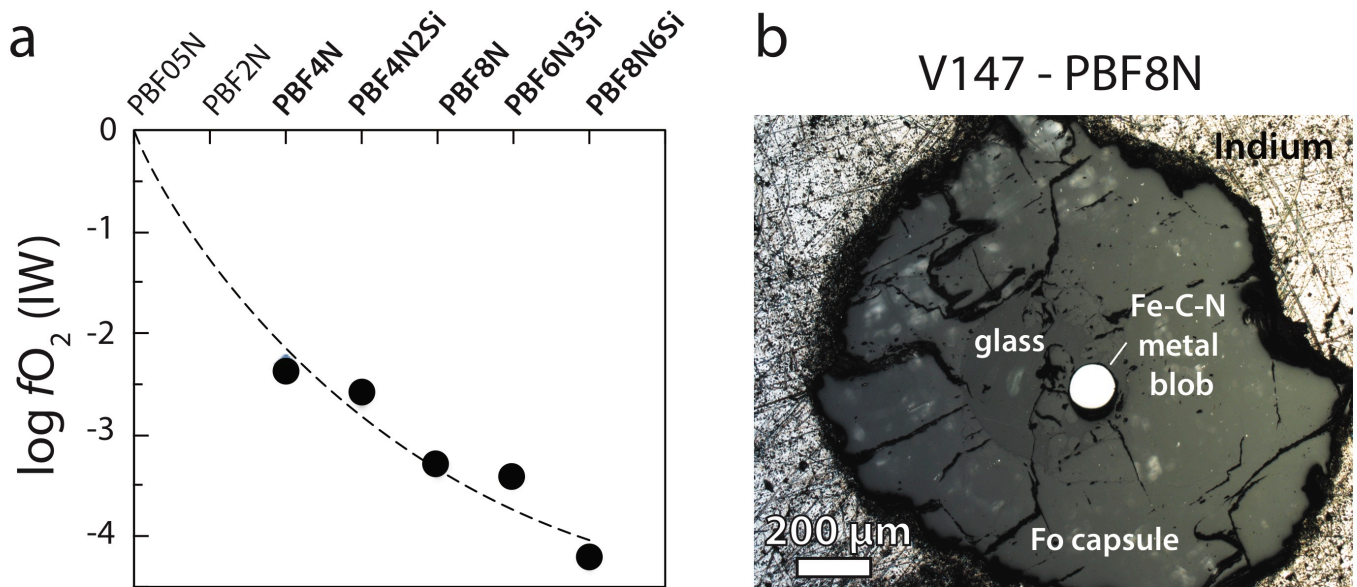


Figure S-3 (a) fO_2 conditions (relative to the IW buffer) calculated for samples containing sufficiently large metal blobs (b). The fO_2 conditions of samples in which metal blobs were too small to be analysed ($<5 \mu\text{m}$) were estimated by extrapolation of the trend, *i.e.*, $\log fO_2$ as a function of the amount of reducing agent (Si_3N_4 and Si metal) added (dashed line, log function).

Supplementary Information References

Aubaud, C., Pineau, F., Hékinian, R., Javoy, M. (2006) Carbon and hydrogen isotope constraints on degassing of CO_2 and H_2O in submarine lavas from the Pitcairn hotspot (South Pacific). *Geophysical Research Letters* 33, L02308.

Bernadou, F., Gaillard, F., Füre, E., Marrocchi, Y., Slodczyk, A. (2021) Nitrogen solubility in basaltic silicate melt—Implications for degassing processes. *Chemical Geology* 573, 120192.

Banerjee, S., Kyser, T.K., Mitchell, R. (2015) Nitrogen isotopic compositions and concentrations in MARID xenoliths. *Chemical Geology* 391, 83–89.

- Boulliung, J., Füre, E., Dalou, C., Tissandier, L., Zimmermann, L., Marrocchi, Y. (2020) Oxygen fugacity and melt composition controls on nitrogen solubility in silicate melts. *Geochimica et Cosmochimica Acta* 284, 120-133.
- Cartigny, P., Harris, J.W., Javoy, M. (2001) Diamond genesis, mantle fractionations and mantle nitrogen content: a study of $\delta^{13}\text{C}$ -N concentrations in diamonds. *Earth and Planetary Science Letters* 185, 85-98.
- Dalou, C., Hirschmann, M.M., von der Handt, A., Mosenfelder, J., Armstrong, L.S. (2017) Nitrogen and carbon fractionation during core-mantle differentiation at shallow depth. *Earth and Planetary Science Letters* 458, 141-151.
- Dalou, C., Füre, E., Deligny, C., Piani, L., Caumon, M.C., Laumonier, M., Boulliung, B., Edén, M. (2019) Redox control on nitrogen isotope fractionation during planetary core formation. *Proceedings of the National Academy of Sciences* 116, 14485-14494.
- De Hoog, J.C., Taylor, B.E., Van Bergen, M.J. (2009) Hydrogen-isotope systematics in degassing basaltic magma and application to Indonesian arc basalts. *Chemical Geology* 266, 256-266.
- de Moor, J.M., Fischer, T.P., Sharp, Z.D., King, P.L., Wilke, M., Botcharnikov, R.E., Cottrell, E., Zelenski, M., Marty, B., Klimm, K., Rivard, C., Ayalew, D., Ramirez, C., Kelley, K.A. (2013) Sulfur degassing at Erta Ale (Ethiopia) and Masaya (Nicaragua) volcanoes: Implications for degassing processes and oxygen fugacities of basaltic systems. *Geochemistry, Geophysics, Geosystems* 14, 4076-4108.
- Fichtner, C.E., Schmidt, M.W., Liebske, C., Bouvier, A.S., Baumgartner, L.P. (2021) Carbon partitioning between metal and silicate melts during Earth accretion. *Earth and Planetary Science Letters* 554, 116659.
- Füre, E., Deloule, E., Dalou, C. (2018) Nitrogen abundance and isotope analysis of silicate glasses by secondary ionization mass spectrometry. *Chemical Geology* 493, 327-337.
- Hauri, E. (2002) SIMS analysis of volatiles in silicate glasses, 2: isotopes and abundances in Hawaiian melt inclusions. *Chemical Geology* 183, 115-141.
- Hirschmann, M.M., Withers, A.C., Ardia, P., Foley, N.T. (2012) Solubility of molecular hydrogen in silicate melts and consequences for volatile evolution of terrestrial planets. *Earth and Planetary Science Letters* 345, 38-48.
- Gerlach, T.M., Taylor, B.E. (1990) Carbon isotope constraints on degassing of carbon dioxide from Kilauea Volcano. *Geochimica et Cosmochimica Acta* 54, 2051-2058.
- Grewal, D.S., Dasgupta, R., Holmes, A.K., Costin, G., Li, Y., Tsuno, K. (2019) The fate of nitrogen during core-mantle separation on Earth. *Geochimica et Cosmochimica Acta* 251, 87-115.
- Iacono-Marziano, G., Morizet, Y., Le Trong, E., Gaillard, F. (2012) New experimental data and semi-empirical parameterization of H_2O - CO_2 solubility in mafic melts. *Geochimica et Cosmochimica Acta* 97, 1-23.
- Javoy, M., Pineau, F., Iiyama, I. (1978) Experimental determination of the isotopic fractionation between gaseous CO_2 and carbon dissolved in tholeiitic magma. *Contributions to Mineralogy and Petrology* 67, 35-39.
- Jugo, P.J., Wilke, M., Botcharnikov, R.E. (2010) Sulfur K-edge XANES analysis of natural and synthetic basaltic glasses: Implications for S speciation and S content as function of oxygen fugacity. *Geochimica et Cosmochimica Acta* 74, 5926-5938.
- Médard, E., McCammon, C.A., Barr, J.A., Grove, T.L. (2008) Oxygen fugacity, temperature reproducibility, and H_2O contents of nominally anhydrous piston-cylinder experiments using graphite capsules. *American Mineralogist* 93, 1838-1844.
- Mikhail, S., Verchovsky, A.B., Howell, D., Hutchison, M.T., Southworth, R., Thomson, A.R., Warbuton, A.P., Jones, A.P., Milledge, H.J. (2014) Constraining the internal variability of the stable isotopes of carbon and nitrogen within mantle diamonds. *Chemical Geology* 366, 14-23.
- Pineau, F., Javoy, M. (1994) Strong degassing at ridge crests: The behaviour of dissolved carbon and water in basalt glasses at 14 N, Mid-Atlantic Ridge. *Earth and Planetary Science Letters* 123, 179-198.
- Renggli, C.J., King, P.L., Henley, R.W., Norman, M.D. (2017) Volcanic gas composition, metal dispersion and deposition during explosive volcanic eruptions on the Moon. *Geochimica et Cosmochimica Acta* 206, 296-311.
- Saal, A.E., Hauri, E.H. (2021) Large sulfur isotope fractionation in lunar volcanic glasses reveals the magmatic differentiation and degassing of the Moon. *Science Advances* 7, eabe4641.



- Shishkina, T.A., Botcharnikov, R.E., Holtz, F., Almeev, R.R., Portnyagin, M.V. (2010) Solubility of H₂O- and CO₂-bearing fluids in tholeiitic basalts at pressures up to 500 MPa. *Chemical Geology* 277, 115-125.
- Speelmanns, I.M., Schmidt, M.W., Liebske, C. (2019) The almost lithophile character of nitrogen during core formation. *Earth and Planetary Science Letters* 510, 186-197.
- Stanley, B.D., Hirschmann, M.M., Withers, A.C. (2014) Solubility of C-O-H volatiles in graphite-saturated martian basalts. *Geochimica et Cosmochimica Acta* 129, 54-76.
- Taylor, B.E. (1986) Magmatic volatiles: isotopic variation of C, H, and S. In: Valley, J.W., Taylor, H.P., O'Neil, J.R. (Eds.) *Stable isotopes in high temperature geological processes. Reviews in Mineralogy and Geochemistry* 16, 185-226.
- Vermeesch, P. (2018) IsoplotR: A free and open toolbox for geochronology. *Geoscience Frontiers* 9, 1479-1493.
- Wade, J., Wood B.J. (2005) Core formation and the oxidation state of the Earth. *Earth and Planetary Science Letters* 236, 78-95.
- Yamamoto, J., Takahata, N., Sano, Y., Yanagita, M., Arai, S., Prikhod'ko, V.S. (2020) Nitrogen and noble gas isotopic compositions of mantle xenoliths from Far Eastern Russia: Implications for nitrogen isotopic characteristics of mantle wedge fluid. *Earth and Planetary Science Letters* 534, 116109.
- Yokochi, R., Marty, B., Chazot, G., Burnard, P. (2009) Nitrogen in peridotite xenoliths: Lithophile behavior and magmatic isotope fractionation. *Geochimica et Cosmochimica Acta* 73, 4843-4861.
- Zhang, C., Duan, Z. (2009) A model for C–O–H fluid in the Earth's mantle. *Geochimica et Cosmochimica Acta* 73, 2089-2102.
- Zhang, H.L., Hirschmann, M.M., Cottrell, E., Newville, M., Lanzirotti, A. (2016) Structural environment of iron and accurate determination of Fe³⁺/ΣFe ratios in andesitic glasses by XANES and Mössbauer spectroscopy. *Chemical Geology* 428, 48-58.

